Oxygen related defects and vacancy clusters identified in sputtering grown UOx thin films by positron annihilation techniques

C. Macchi [a], A. Somoza [a,*], J. Guimpel [b], S. Suárez [b], W. Egger [c], C. Hugenschmidt [d], S. Mariazzi [e], R.S. Brusa [e,*]

[a] CIFICEN (UNCPBA-CICPBA-CONICET) and Instituto de Física de Materiales Tandil (UNCPBA), Pinto 399, B7000GHG Tandil, Argentina
[b] Comisión Nacional de Energía Atómica - Centro Atómico Bariloche, CONICET and Instituto Balseiro-Universidad Nacional de Cuyo, Avda Bustillo 9500, San Carlos de Bariloche 8400, Argentina
[c] Universität der Bundeswehr (München) und Institut für Angewandte Physik und Messtechnik, LTR 2 Werner Heisenberg Weg 39, 85577 Neubiberg, Germany
[d] Physik-Department E21 and FRMII, Technische Universität München, Lichtenbergstrasse 1, 85748 München, Germany
[e] Department of Physics, University of Trento and TIFPA-INFN, via Sommarive 14, I-38123 Povo, Trento, Italy

ABSTRACT

We experimentally studied the formation of vacancy clusters and oxygen related defects in uranium oxide (UOx) thin films (<70 nm) changing the stoichiometry in the x = 2.2–3.5 range. Films were deposited on Si(0 0 1) by DC magnetron sputtering varying the substrate temperature (room temperature, 400 °C and 600 °C) and different relative O_2 partial pressures in the argon-oxygen mixture. The different species of vacancy-like defects are identified by the combination of depth dependent positron annihilation techniques and by comparison of the experimental data with *ab-initio* calculations. In samples growth up to 400 °C substrate temperature, di- and tri-vacancies were formed whereas at higher temperature, hexa-vacancies and larger vacancy clusters appear. Film growth at increasing oxygen partial pressure was found not to be correlated with an increase of oxygen defects, but with the formation of more complex vacancy clusters. The presence of oxygen related defects is revealed by identifying preferential positron annihilations with oxygen electrons. Moreover, uranium vacancies inside vacancy clusters are identified by localization of positrons, in agreement with *ab-initio* calculations.

Introduction

Uranium dioxide (UO2) is mainly used as fuel in nuclear fission reactors. Under different conditions of oxygen pressure and temperature, UO2 moves away from its ideal fluorite stoichiometry composition by including excess oxygen atoms [1]. Uranium oxide grown as thin films is beneficial for several applications. For example, the possibility of using uranium oxide/iron oxide heterojunctions as water oxidation catalyst [2] or for solar cell applications [3] has been studied. In addition, the oxides as thin film samples – not as bulk material –would be needed for stopping power determination based on Rutherford backscattering (RBS) measurements [4]. To the best of our knowledge, there are only two experimental references of stopping power measurements of ions in uranium oxides [5,6].

The study of defects in stoichiometric and hyperstoichiometric uranium dioxide is of fundamental interest for improving the fuel performance and behavior under normal operation. Defects impact on all engineering aspects regarding the fuel elements in the different stages of their life: production stage, in reactor operation and finally when they are stored as used elements. In fact, defects impact on the thermal and electrical conductivity of fuel elements [7-9], radiation damage and fission gas release [10-13].

In hyperstoichiometric uranium dioxide $UO_{x>2}$, oxygen is mainly incorporated in the lattice as interstitial point defects [14-19]. It was reported that, for increasing x values, these defects interact and form unstable interstitial clusters [16,17,19]. As a consequence of the lack of uranium and/or oxygen atoms, neutral and charged vacancies and vacancy clusters can also be present [15-17]. The oxygen diffusion, as well as vacancies, contribute to the formation of O-vacancy-like complexes [15,19].

In real systems, due to the presence of different valence states with similar energies accessible to the uranium atoms, a coexistence of several types of defects, such as interstitials oxygen clusters and vacancy clusters with different charge states, was predicted. In particular, it was

* Corresponding authors.
E-mail addresses: asomoza@exa.unicen.edu.ar (A. Somoza), robertosennen.brusa@unitn.it (R.S. Brusa).

reported that oxygen and uranium monovacancies, as well as vacancy clusters containing different number of uranium and/or oxygen vacancies, have charges from 0 to -8 [20]. Although detailed DFT + U *ab-initio* calculations [7,10,16-22] enabled the prediction of different defect types as well as their charges and their stabilities, it is demanding to get detailed experimental information regarding these defects.

Positron annihilation spectroscopy (PAS) has demonstrated to be a powerful experimental technique highly sensitive to vacancy-like defects in solids [23,24]. Moreover, PAS in its three experimental variants, viz., Positron Annihilation Lifetime Spectroscopy (PALS), Doppler Broadening Spectroscopy (DBS) and Coincidence Doppler Broadening Spectroscopy (CDBS), made it possible to obtain defect profiles in thin films when using an energy tunable slow positron beam (pulsed for PALS [25] and continuous for DBS and CDBS [26]).

Positrons entering in asample slow down to thermal energies within a few picoseconds by ionization and excitation in the solid. The thermalized positrons then diffuse through the lattice until they are trapped in regions of significantly lower-than-average electron density, such as vacancies and vacancy clusters, where they subsequently annihilate with electrons. Due to their positive charge, positrons are favorably trapped in neutral or negatively charged vacancy sites. Positron lifetimes and momentum distributions differ significantly in the defect and in the defect-free lattice. Studies of the changes in the mentioned parameters provide information on the size of the positron traps and the chemical environment of the annihilation site.

In the literature, there is scarce information regarding the study of point-like and vacancy cluster defects in UO_2 samples using PAS. Two works on this issue were published; in the first one, a study of defects was carried out using *ab-initio* calculations of the momentum distributions of annihilating electron–positron pairs [22]. In the second paper, PALS was used to study vacancy-like defects introduced in UO_2 during α irradiation [21]. For their interpretation, the authors corroborated the experimental results by DFT + U calculations.

In this work, PALS, DBS, and CDBS were used to depth profile point-like defects in UO_x thin films grown on Si(001) subtrates dependent on the different experimental conditions, *i.e.*, substrate temperatures and/or oxygen partial pressures in the sputtering gas.

Experimental methods

Samples

The UO_x thin films were grown on Si(001) substrates by DC magnetron sputtering, starting from a stoichiometric sintered U_3O_8 target. The substrates were cut from standard commercial wafers and attached to a resistive heater [27] with Ag paste, which allowed for heating up to 700 °C. The substrate temperature, Ts, was measured and controlled with a thermocouple in direct thermal contact with the substrate backside. The base pressure of the sputtering system was 4×10^{-4} Pa (3×10^{-6} Torr). The sputtering gas was a mixture of 99.999% pure Ar and 99.995% pure O_2. The total pressure during growth was controlled at 2.67 Pa (20mTorr) with a gas composition that was varied for different films. Films were grown for relative O_2 partial pressures, RP $(O_2) = P(O_2)/2.67$ Pa, equal to 0 (pure Ar), 0.1, and 0.2. Table 1 lists the film labels and growth parameters. Two series were grown, one with pure Ar as sputtering gas (UO-1, UO-2, and UO-3) and varying Ts, the other for Ts = 400 °C and varying RP(O_2) partial pressure (UO-2, UO-4, and UO-5). For the UO-1 film, the deposition was done without heating the substrate, but due to the deposition, the substrate temperature raised from room temperature (RT) to 115 °C. The UO-2 and UO-3 films were grown at substrate temperatures of 400 °C and 600 °C, respectively. The second series of films were grown at different O_2 partial pressure ratios in the sputtering gas, ranging from 0 to 0.2 (UO-2, UO-4, and UO-5).

X-Ray diffraction (XRD), and low angle X-Ray Reflectivity (XRR) patterns were measured at room temperature (RT) on a PANalytical Empyrean diffractometer in Bragg-Brentano geometry with Cu-Kα ra-

Table 1
Growth conditions of the UO_x film samples: substrate temperature T and O_2 partial pressures to total pressure ratio (RP(O_2)); total thickness t [nm] and lattice parameter d [nm] (for details see text).

Temperature T→	30–115 °C	400 °C	600 °C
RP(O_2)(O_2 partial pressure ratio) ↓			
0	UO-1	UO-2	UO-3
	t = 68.9 ± 0.1	t = 59.2 ± 0.1	t = 37.1 ± 0.2
	d = 0.321 ± 0.005	d = 0.317 ± 0.005	d = 0.313 ± 0.005
0.1		UO-4	
		t = 64.6 ± 0.2	
		d = 0.416 ± 0.005	
0.2		UO-5	
		t = 60.4 ± 0.1	
		–	

diation, i.e. with a wavelength $\lambda = 0.15418$ nm. The samples were mounted in a 4-circle Eulerian cradle, which allowed for precise alignment at low angles. Film thicknesses were determined through the periodicity of the low-angle Kiessig fringes in the XRR measurements [28]. These intensity oscillations are due to the interference of reflections from the surface of the film and the film-substrate interface. At the low angle region, the effect of X-ray refractive index cannot be neglected. It can be expressed as n = 1-δ, with $\delta \ll 1$ being proportional to the electron density of the material. Since the electron density of Si is smaller than that of UO_x, there is a π phase change on the reflection at the film-substrate interface. Taking into account these facts, the peak positions in the reflected intensity can be expressed as

$$sin^2\theta_n = \left(n + \frac{1}{2}\right)^2 \left(\frac{\lambda}{2t}\right)^2 + 2\delta \qquad (1)$$

where θ_n is the position of the n-th order maximum, n = 0,1,2,…, λ is the X-ray wavelength (0.15418 nm for Cu-Kα radiation) and t is the film thickness. In the main panel of Fig. 1, the experimental data obtained for the UO-5 film are shown as intensity *versus* 2θ scan. In the inset, the evolution of $sin^2(\theta)$ as a function of $(n+\frac{1}{2})^2$ at the intensity maxima is presented. As can be seen, a linear relation is observed as predicted by Eq (1). The results for the thicknesses of the film are reported in Table 1.

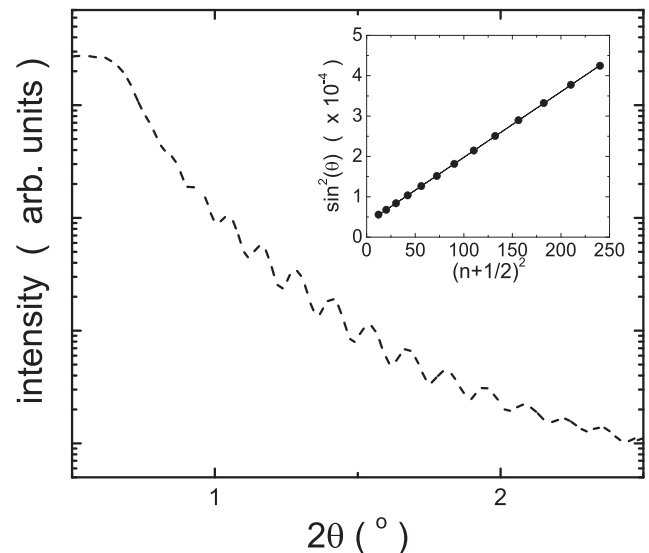In Fig. 2 the XRD diffractograms for allgrown UO_x films are

Fig. 1. Low angle X-ray reflectivity data obtained for the film UO-5. The inset presents the evolution of $sin^2(\theta)$ as a function of $(n+\frac{1}{2})^2$.
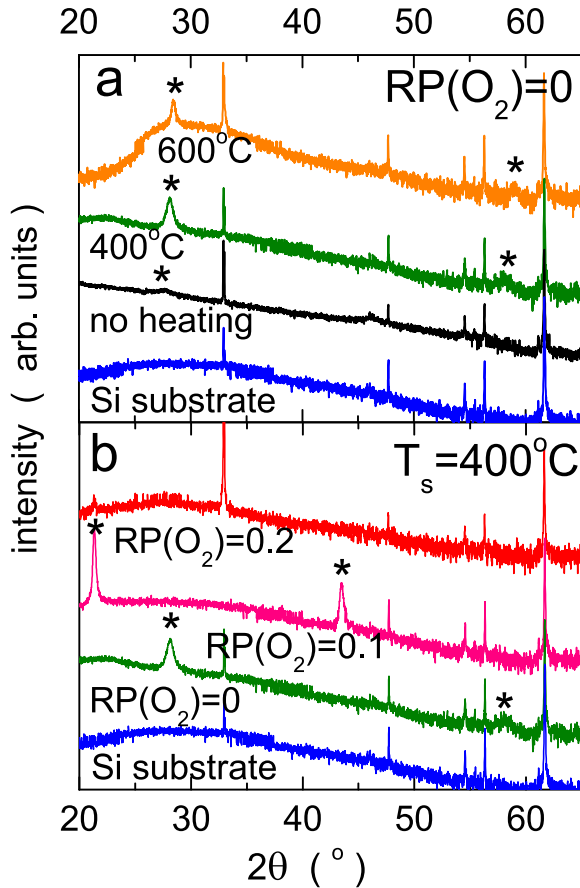
Fig. 2. X-ray diffractograms for all UO$_x$ films. (a) samples prepared at different substrate temperatures and with Ar as sputtering gas. (b) samples prepared at 400 °C and at different relative O$_2$ partial pressure, RP(O$_2$). In both panels, the diffractogram obtained for a Si(0 0 1) substrate is presented. Peaks related to UO$_x$ films are marked with an asterisk.

presented. The top panel (a) shows the XRD data obtained for the films grown at different substrate temperatures and for constant RP(O$_2$). In the bottom panel (b), the evolution of the structure of the film with RP(O$_2$) for constant Ts is shown. For all films, two peaks are observed, the higher angle peak being the second order of the low angle one, which signals textured growth of the oxide. The only exception is UO-5 (Ts = 400 °C and RP(O$_2$) = 0.2), for which no UO$_x$ related peaks could be identified. The lattice parameters, d, obtained from the peak positions are reported in Table I. Unfortunately, the single value of d for each film is not enough to identify the structure since many compatible values can be found among the different UO$_x$ phases. As can be seen in Table I, two clear trends can be identified. While the lattice parameter reduces for increasing substrate temperatures; it seems to increase very fast when the relative O$_2$ partial pressure increases.

The ratio of oxygen to uranium composition, x, was measured by Rutherford Backscattering Spectrometry (RBS) [29] using the 1.7 MeV tandem accelerator, 5SDH Pelletron NEC, located at the Centro Atómico Bariloche, Argentina [30]. Samples were bombarded by a 2 MeV ^{4}He-beam. It is considered that these particles collide elastically with the target atoms and get scattered with an energy characteristic of the mass of the dispersing center. In addition, they lose energy as they travel inside the material both, during entering and leaving the sample. The dispersed particles are detected in backward directions, corresponding to scattering angles greater than 90°, with a surface barrier detector. In our setup, we fixed the detection angle at 165°. The energy spectrum of the detected particles contains information on the composition of the

target and on the distribution in depth of the constituent elements. The SIMNRA computer code was used to analyze the spectra generated by RBS [31]. Fitting the obtained spectra with the SIMNRA code enables the determination of the atomic stoichiometry of the samples within uncertainties of the order of 2%.

Fig. 3 shows the relative O$_2$ partial pressure dependence of the oxygen to uranium ratios, determined from SIMNRA fit to the RBS data. The x versus RP(O$_2$) behavior is indeed reasonable, showing a larger O content for larger RP(O$_2$). However, a non-clear systematic is observed as a function of substrate deposition temperature at RP(O$_2$) = 0. An interesting fact is that the O/U values for RP(O$_2$) different from 0 are close to 3.5, i.e. a value for which no stable uranium oxide has been reported in the literature.

Positron annihilation Spectroscopy

Positron annihilation spectroscopy measurements were carried out at the high intensity positron source NEPOMUC (NEutron induced POsitron source MUniCh) [26,32] at the research neutron source Heinz Maier-Leibnitz (FRM II) of the Technical University of Munich. PALS for positron depth profiling was measured in the 1 to 18 keV positron implantation energy range using the Pulsed Low Energy Positron System (PLEPS) [25]. It is important to point out that the implantation energy E is related to the mean positron implantation depth $< z >$ by the equation

$$< z > = \frac{40}{\rho} E^{1.6} \qquad (2)$$

where $< z >$ is expressed in nm, the density of the samples ρ is given in g/cm^3 and E in keV [33].

The overall time resolution of the PALS spectrometer (pulsing and detector) was 230–240 ps and the beam diameter of about 1 mm at all energies. Lifetime spectra $F(t)$ typically containing 4×10^6 counts were acquired. A PALS spectrum is the convolution of a resolution function $R(t)$ with a sum of exponential functions expressed as:

$$F(t) = R(t) \otimes \sum_i \frac{I_i}{\tau_i} \exp\left(\frac{-t}{\tau_i}\right) + BG \qquad (3)$$

where τ_i and I_i are the lifetime and its associated intensity of the positron annihilating in the state i and BG is the background. To get the
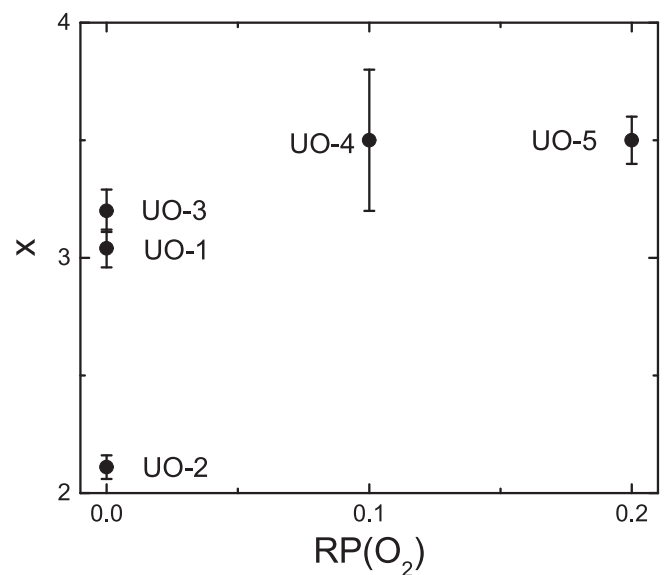

Fig. 3. Oxygen to uranium concentration ratio, x, obtained from RBS measurements and SIMNRA simulation, as a function of the relative O$_2$ partial pressure in the sputtering gas, RP(O$_2$) = P(O$_2$)/2.67 Pa. Error bars indicate the dispersion for the measured values in different regions of the film.

positron lifetimes and their respective intensities, the acquired spectra were analyzed using the POSFIT package [34]. In the present work, the obtained PALS spectra were satisfactorily deconvolved by considering three lifetime components.

Doppler Broadening Spectroscopy (DBS) and Coincidence Doppler Broadening Spectroscopy (CDBS) measurements were carried out using an experimental set-up with four high purity Ge detectors (30% efficiency, energy resolution 1.3 keV at 477.6 keV [35]) that were used independently in the case of DBS or in coincidence mode for CDBS. Detectors are kept tilted with respect to the sample surface in order to reduce losses in the conting rate due to the absortion or scattering of the positron–electron annihilation radiation by the sample.

In the same way of PALS, DBS measurements of the positron–electron annihilation line were performed at different positron implantation energies. The recorded 511 keV annihilation line in the laboratory frame is Doppler broadened due to the motion of the electron–positron pair. The longitudinal momentum component p_L with respect to the detector direction is related to the energy shift by $p_L = 2\Delta E/c$; where $\Delta E = |E_\gamma - 511\ keV|$ with E_γ being the energy of the detected gamma quanta. Before its annihilation, a positron reaches the thermal energy of the lattice; therefore, its momentum is negligible compared to the electron momentum. As a consequence, the broadening of the annihilation peak can be considered as only due to the electron momentum. The shape of the annihilation line hence corresponds to a one-dimensional electron momentum distribution convoluted with the detector resolution function. The low momentum region of the annihilation peak ascribed to positron annihilation with valence electrons is characterized by the so-called shape parameter S. This parameter is defined as the area of the central low-momentum part of the peak divided by the area below the whole curve, after background subtraction. The energy windows chosen to calculate the S parameter were $|511\ keV - E_\gamma| <0.91$ keV and $|511\ keV - E_\gamma| <4.25$ keV for the central and the total area of the annihilation line, respectively. On the other hand, the high-momentum region of the peak corresponds to positron annihilation with core electrons.

As mentioned above, the DBS technique produces fast and very useful data regarding the spectrum of valence electrons and high-momentum core electrons. Owing to the low peak-to-background ratio, a DBS spectrum hardly gives any information on inner core electrons, which contribute predominantly to the high-momentum tails of the spectrum. However, this is valuable information, because core electrons retain their atomic character even in a solid, thus they can provide a chemically specific signal in the momentum distribution. This information can be obtained using CDBS technique which not only increases the peak-to-background ratio, roughly by three orders of magnitude but also improves the energy resolution by a factor $\sqrt{2}$ in comparison to that of a single detector [36-39]. However, to get reliable CDBS data requires long measurement times. Therefore, our measurements of the UOₓ films were done at the selected implantation energy 3 keV. The effective resolution of the CDBS spectrometer in the coincidence mode is 1.1 keV at a gamma energy of 511 keV (for details, see Ref. [40,41]). The CDBS technique has demonstrated to be very sensitive to the chemistry of solids and to the presence of lattice defects. For studies aiming at the chemical analysis of the annihilation sites, it is convenient to enhance the high-momentum tails. In such a way, the core electrons can be detected. In order to enhance the details of the spectra in the high-momentum region, which is most important for the identification of the chemical species in contact with vacancy-like defects, the data can be shown in terms of the relative differences to a reference curve [37,38,42,43]. In the present work, the CDBS data are presented as CDB ratio curves relative to the UO-2 and then UO-5 sample as references, respectively (see next Section). In the following, the statistical noise of the experimental data was reduced by averaging groups of three adjacent points in the range between ~ 0.7 to 1.4 atomic momentum units and of six adjacent points for momentum values above 1.4 atomic units.

Results and discussion

Doppler Broadening Spectroscopy

Depth profile DBS measurements were employed to characterize the distribution of the vacancy-like defects as a function of the depth of the deposited film. Detailed information about the defect distribution can be gained from the experimental data using a simple model based on the solution of the positron stationary diffusion equation [44-46]. Specifically, in this work, the VEPFIT program was used [44].

In Fig. 4(a) and 4(b), the line shape parameters S_n as a function of the mean positron implantation depth for the two series of samples are shown. The measured $S(E)$ values were normalized to the S value obtained for bulk Si ($S_b = 0.588$): $S_n(E) = S(E)/S_b$. This normalization allows the comparison with the data obtained in other laboratories [32].

When using the VEPFIT program to analyze the data, the thickness of the UOₓ films was fixed using the values obtained by X-ray reflectivity (see Table 1) and a density of the films equal to 10.97 g/cm³ as reported in the literature for UO₂ [47]. In all the cases, the DBS curves were satisfactorily fitted considering four layers: a superficial layer, two layers assigned to the film, and the fourth layer corresponding to the Si substrate. It was found that the superficial layer had thicknesses of only few nanometers. Since this layer does not contain useful information on the internal structure of the films, from now on, it will not be taken into account for further analysis of the DBS curves.

In Table 2, the values of S_n, the thickness of the respective layers Δ, and the diffusion length L_+ in the two layers are reported. At each positron implantation energy E, the values of $S_n(E)$ can be expressed as a linear combination of the S_s, S_b and S_{di} values, which are characteristic of the positron annihilation in the surface, the bulk, and the different i defect-states, respectively:

$$S_n(E) = S_s f_s(E) + S_b f_b(E) + \sum_i S_{di} f_{di}(E) \qquad (4)$$

where $f_s(E)$, $f_b(E)$ and $f_{di}(E)$ are the fractions of positrons annihilating at the surface, in the bulk and in i defect-states, respectively. The very low L_+ values, some of them compatible with 0 within the errors, obtained for the deposited films (see Table 2) indicate that all positrons are annihilating in vacancy-like positron trapping sites (so-called saturation trapping regime, see also the discussion of PALS results below). As a consequence, at energies above 1 keV, $f_b(E)$ as well as $f_s(E)$ are negligible and, therefore, Eq. (4) reduces to $S_n(E) \cong \sum_i S_{di} f_{di}(E)$.

As can be seen in Table 2, independently of the UOₓ film growing conditions, the first layer presents S_n values lower than those obtained for the second layer. According to PALS results (see next paragraph), the diverse values of S_n parameter can be associated with the presence of different types and concentrations of defects in the two layers.

Positron Lifetime Spectroscopy

From the analysis of the obtained PALS spectra, it was found that the values of the third lifetime component are around 2.5 ns. The associated intensity values are very small; they are strongly dependent on the positron implantation energy; e.g., from $I_3 = 1\%$ for 3 keV to $I_3 = 0.2\%$ for 6 keV. This lifetime component corresponds to pick-off annihilation of o-Ps formed by back-diffused positrons reaching the surfaces of the film. As the aim of the present work is to study the depth profiling of defects in thin films, the long-lived lifetime component does not bring any useful information. For this reason, the analysis and discussion of PALS data will be focused on the first and second lifetime components.

In Fig. 5, the lifetimes τ_1 and τ_2 and their associated intensities obtained from the measurements for the films growth at different substrate temperatures (UO-1, UO-2, and UO-3 samples) are presented as a function of the positron implantation energy. In the figure, the dashed vertical lines in all panels indicate the different layers detected in the film (labeled I and II) and the Si substrate as found by fitting the DBS
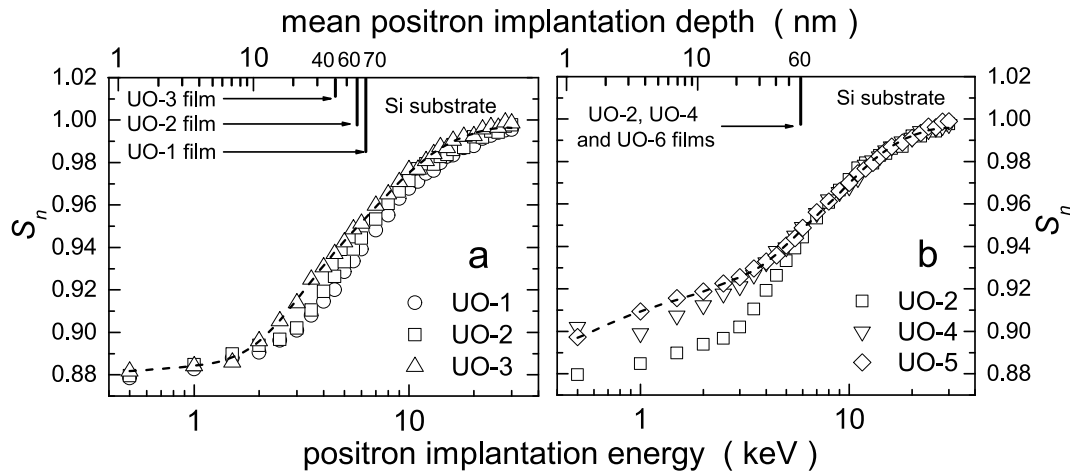
Fig. 4. Line shape parameter S_n as a function of the positron implantation energy (lower scale) and the mean positron implantation depth in each film (upper scale). (a) data of samples grown at different substrate temperatures. (b) data for the series of samples deposited onto the substrate at different gas mixture composition. Error bars are within the symbols. In both panels, the dashed lines through the experimental data points were obtained using the VEPFIT program (see text). For the sake of clarity, only two best fits are presented (dashed lines). Vertical marks point out the end of the film for each UO_x sample.

Table 2

Characteristic parameters of the two layers corresponding to the film obtained by means of VEPFIT analysis of the DBS depth profiles on UO_x films grown under different substrate temperatures (UO-1 – UO-3), and grown under different O_2 partial pressures to total pressure ratio (UO-2, UO-4, UO-5). Δ is the thickness of the respective layers and L_+ the positron diffusion length. The error associated with S_n is $\pm$ 0.001.

Sample	Layer I			Layer II		
	S_n	Δ (nm)	L_+ (nm)	S_n	Δ (nm)	L_+ (nm)
UO-1	0.889	23	2^{+2}_{-2}	0.942	46	13 ± 5
UO-2	0.896	38	5 ± 3	0.949	21	1^{+4}_{-1}
UO-3	0.885	14	2^{+3}_{-2}	0.951	23	10 ± 3
UO-2	0.896	38	5 ± 3	0.949	21	1^{+3}_{-1}
UO-4	0.904	17	11 ± 5	0.950	48	20 ± 10
UO-5	0.918	18	2^{+3}_{-2}	0.947	42	15 ± 5

curves.

In Fig. 6, the same positron lifetime parameters reported in Fig. 5 are presented but they were obtained from the measurements for the films growth at 400 °C, and for different O_2 partial pressures (UO-2, UO-4, and UO-5). In the upper left panel of Fig. 5, the solid and the dashed curves represent the positron implantation profiles calculated for positrons implanted at 3 and 6 keV, respectively. As can be seen, some of the positrons implanted at energies higher than 3 keV are annihilated in the Si substrate.

In order to investigate changes of the lifetime data at implantation energies above 3 keV, we have measured the sample UO-2, having a ratio of oxygen to uranium composition very close to the stoichiometry, up to an energy of 18 keV. As can be observed, the panel labeled UO-2 in Figs. 5 and 6, for energies equal or higher than 6 keV, positrons begin to probe the Si substrate. The first positron lifetime obtained for the UO-2 sample is almost constant up to $E = 4$ keV, while its associated intensity increases from 20% up to roughly 30%. Increasing the positron implantation energy, i.e., smearing the positron implantation profile and increasing the mean positron implantation depth, up to 18 keV, the τ_1 value increases up to 200 ps with $I_2 \sim 80\%$. This lifetime value approaches that measured in Si single crystal of 220 ± 3 ps as was widely reported in the literature [48]. The second lifetime remains almost constant at around 350 ps but its intensity starts to decrease from about 70% at a positron implantation energy of 4 keV to 20% at 18 keV

indicating that positrons of higher energy probe the defected layers of the films to a lesser extent.

In the light of the above results, we have performed PALS measurements for all samples at positron implantation energies of 1, 2 and 3 keV, corresponding to a mean positron implantation depth of approximately 4, 12 and 23 nm, respectively. For these energies, the vast majority of the implanted positrons annihilate in the UO_x layers.

As can be seen in Figs. 5 and 6, the lifetime values measured at an implantation energy of 1 keV, are on the average higher than those measured at 2 and 3 keV. This result is attributed to the non-negligible contribution of positron annihilations in surface states as a consequence of the positron diffusion length (see Table 2, first layer) comparable to the mean positron implantation depth.

In Table 3, we have reported the lifetimes and their associated intensities obtained from the measurements for the samples at an implantation energy of 2 and 3 keV. In the measurements carried out on the UO-1 sample at 2 and 3 keV, more than 90% of the positrons implanted probe the first layer; consequently, the data reported correspond to the lifetime components measured in the first layer. For the sample UO-2, the positron lifetimes and their associated intensities in the second layer were assumed to be the mean values between those measured at 3 and 4 keV. For the samples UO-3, UO-4, and UO-5 at an implantation energy of 2 keV, positrons mainly probe the first layer, while at 3 keV, approximately 50% of positrons probe the second layer. As can be seen in Table 3, in general the lifetime values of the second layer for all samples are higher than those obtained for the first layer; the same trend is observed in the corresponding S values obtained from the DBS measurements (see Table 2).

The first step of the analysis of the evolution of the PALS data is focused on the results obtained for the sample UO-2 which has a nearly stoichiometric composition. For positrons implanted into the UO-2 film (considering the layer I as well as the layer II), the short-lived lifetime remains constant, within the experimental scatter, at 174 ± 4 ps. The second lifetime increases from approximately 300 ps in the layer I up to about 325 ps in the layer II; while in this energy range the intensity associated with τ_2 decreases from 76% to 72%.

From the PALS results obtained for the samples grown at different substrate temperatures (see Fig. 5 and Table 3), within the experimental scatter, a constant τ_1 value of ~ 179 ps on the average is found for both layers. Besides, the associated intensities I_1 are almost the same in the two layers for each sample but they systematically increase from about 17% to 33% with the increase of the substrate temperature. Regarding the τ_2 values measured in the layer I, a significant lifetime increase is
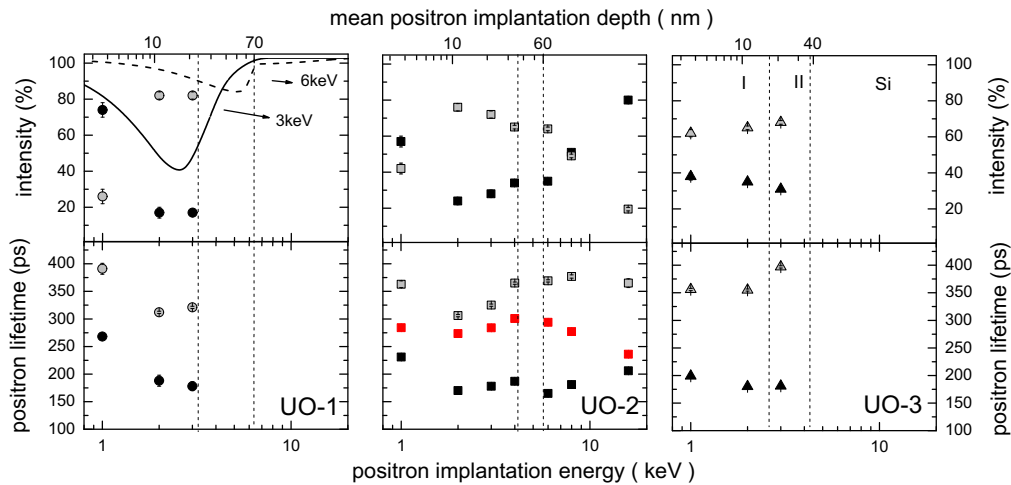
Fig. 5. Positron lifetime parameters (τ_i and I_i) as a function of the positron implantation energy (lower scale) and the mean positron implantation depth (upper scale) for the series of samples grown at different substrate temperatures. Full symbols: τ_1 and I_1; Open symbols: τ_2 and I_2. and full red squares represent the mean positron lifetime. The regions separated by the vertical dashed lines correspond to the different layers detected in the film (labeled I and II, respectively) and the Si substrate. In the first panel, the solid and the dashed curves represent the positron implantation profiles calculated for positrons implanted at 3 and 6 keV, respectively. In the case of those data points in which the error bars cannot be seen, the errors are within the symbol. (For interpretation of the references to colour in this figure legend, the reader is referred to the web version of this article.)
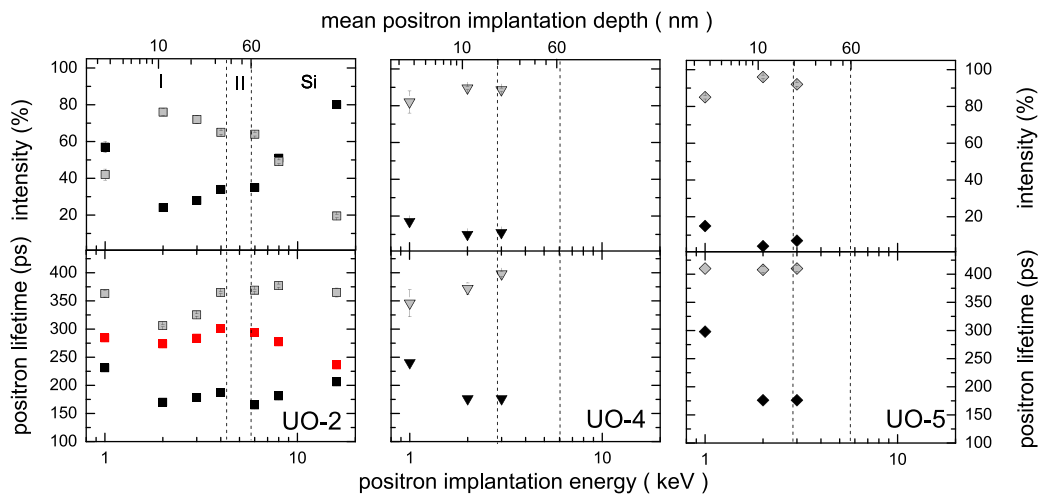

Fig. 6. Positron lifetime parameters (τ_i and I_i) as a function of the positron implantation energy (lower scale) and the mean positron implantation depth (upper scale) for the series of samples deposited onto the substrate at different gas mixture composition. Full symbols: τ_1 and I_1; Open symbols: τ_2 and I_2, and full red squares represent the mean positron lifetime. The regions separated by the vertical dashed lines correspond to the different layers detected in the film (labeled I and II, respectively) and the Si substrate (see text). In the case of those data points in which the error bars cannot be seen, the errors are within the symbols. (For interpretation of the references to colour in this figure legend, the reader is referred to the web version of this article.)

observed for the film grown at 600 °C with respect to those obtained for the films grown at lower temperatures; specifically, 355 ps *versus* 316 ps. A similar behavior is observed in layer II; 397 ps against 325 ps.

In the case of the PALS data presented in Fig. 6 and Table 3 obtained for the films grown at 400 °C and for different O_2 partial pressures, τ_1 values corresponding to layer I and II are for all samples practically the same, i.e., 176 ± 5 ps on the average. In this case, in each sample, the intensity values measured in the layer I and II, do not differ significantly. However, a systematic decrease of the intensities from $\sim 28\%$ to $\sim 4\%$ is observed when the O_2 partial pressures increases. For this series of samples and taking into account the two layers, a progressive increase of the τ_2 values with the increment of the O_2 partial pressures is observed.

On the other hand, an average of the short lifetimes measured for all samples is made, the obtained $\tau_1 = 177 \pm 5$ ps is slightly higher than the

experimental bulk positron lifetime reported by M.F Barthe *et al.* [49] for well-polished and annealed samples of UO_2, i.e.$\tau_b = 169\pm1$ ps. This lifetime value is in good agreement with those obtained for UO_2, by means of DFT + U *ab-initio* calculations using different schemes, 167 and 168 ps [21]. These authors also reported an experimental positron lifetime of 170 ± 5 ps from measurements of UO_2 samples irradiated with 45 MeV α particles in the temperature range between 15 and 300 K. It was also reported that this τ_1 value was independent of the temperature; the authors associated this lifetime component with positron annihilations in negatively charged interstitial oxygen. For samples having also vacancy-like defects, a short lifetime higher than the characteristic lifetime of the UO_2 bulk is expected. Taking into account the experimental average τ_1 value obtained in the present work, and based on the results reported in Ref. [21], our first lifetime component can be

Table 3
PALS results obtained for the samples of the UO_x films grown under different substrate temperatures (UO-1 – UO-3) and grown under different O_2 partial pressures to total pressure ratio (UO-2, UO-4, UO-5).

Sample	First component				Second component			
	First layer		Second layer		First layer		Second layer	
	τ_1 (ps)	I_1	τ_1(ps)	I_1	τ_2(ps)	I_2	τ_2(ps)	I_2
UO-1	183 ± 8	17 ± 2	–	–	316 ± 4	82 ± 1	–	–
UO-2	170 ± 5	24 ± 2	178 ± 5	28 ± 2	306 ± 5	76 ± 1	325 ± 5	72 ± 1
UO-3	180 ± 5	35 ± 2	181 ± 5	31 ± 2	355 ± 5	65 ± 1	397 ± 4	69 ± 1
UO-2	170 ± 5	24 ± 2	178 ± 5	28 ± 2	306 ± 5	76 ± 1	325 ± 5	72 ± 1
UO-4	176 ± 4	10 ± 2	176 ± 4	11 ± 2	370 ± 5	90 ± 1	398 ± 5	89 ± 1
UO-5	176 ± 4	4 ± 2	176 ± 4	7 ± 2	408 ± 5	96 ± 1	410 ± 5	92 ± 1

attributed to positron annihilation near negatively charged non-vacancy defects. Specifically, this non-vacancy defects were assumed to be negative oxygen mono-interstitials and interstitial clusters. In fact, from experimental studies previously carried out on the oxygen diffusion in UO_2 it was suggested that oxygen interstitials were doubly charged [7]. In a further study on the charge states of defects in uranium oxide calculated using a local hybrid functional for correlated electrons, it was reported that oxygen interstitials were non-neutral with a − 2 charge [20]. Also, from experimental and theoretical studies of UO_{2+x}, it was suggested that, besides mono-interstitials, there exist different types of negatively charged O defects such as di-interstitials or oxygen clusters [16,17]. In a similar way, J. Wang et al. [14] have proposed that, in the average structure of UO_{2+x}, a combination of all these defects could be the most likely effective trapping sites for positrons.

Regarding the second lifetime values reported in this work for all samples, they vary between 300 and 400 ps, while their associated intensities change between ∼ 60 and ∼ 90%. All these τ_2 values are much higher than τ_b. Since isolated oxygen vacancies in UO_2 are predicted to have positive charges associated with them [16,17], they are not effective positron traps. Conversely, neutral and negatively charged oxygen vacancies trap positrons and an associated positron lifetime around 200 ps was reported [21]. Consequently, the second lifetime component obtained in the present work can be associated with positron annihilation in uranium vacancies (V_U) and vacancy clusters, as discussed below.

Detailed DFT + U lifetime calculations of positrons trapped in neutral and charged uranium (V_U) and oxygen (V_O) vacancies, in complexes from di-vacancies to hexa-vacancies: ($V_U + V_O$), ($V_U + 2V_O$), ($2V_U + 2V_O$), ($2V_U + 4V_O$), in different configurations and with different charge states were performed [21]. Positron lifetime calculations carried out using two different calculation schemes were found to differ by few picoseconds (details about calculations are given in Ref. [21]. Hence, the positron lifetime calculated for neutral and negative V_O ranges from 195 ps to 206 ps, while for V_U, the lifetime varies between 289 ps and 304 ps. For vacancy clusters (up to hexa-vacancies), the lifetime values vary from 300 ps to 365 ps. Many vacancy configurations have very similar positron lifetimes; for example, for tri-vacancies the lifetime values vary between 301 ps and 316 ps, and for tetra-vacancies with a 4- charge, the corresponding positron lifetime ranges from 309 ps to 319 ps. The positron lifetime for a neutral tetra-vacancy (324 ps-339 ps) is very similar to that obtained for a neutral hexa-vacancy (323 ps-329 ps). The delimited range of variation of the positron lifetimes in the different configurations of vacancy clusters was explained by the fact that the positron wave function mainly localizes in V_U or in between two V_U, while it is slightly affected by the presence of one or more V_O [21].

For this reason, in the samples studied in the present work, the

measured lifetime τ_2 cannot be directly associated with a specific vacancy cluster. In fact, it cannot be excluded that this lifetime value is an average of the contribution of positron annihilations in different types of vacancy clusters which, as mentioned above, have similar lifetime values. Specifically, taking into account the experimental second lifetime values reported in Table 3 and, also considering the calculated positron lifetimes reported by Wiktor et al. [21], it can be said that the measured τ_2 in the UO-1 and UO-2 samples is compatible with a vacancy cluster containing different types of di- and tri-vacancies; that is, 2 V_U^8, 2 V_U^0, $(V_U + V_O)^0$, $(V_U + V_O)^{-2}$ and $(V_U + 2V_O)^0$. Besides, in the case of the UO-3 sample, the vacancy clusters in the samples are compatible with the presence of $2V_U + 4V_O$ or bigger vacancy clusters. Finally, the τ_2 values obtained from the measurements of the UO-4 and UO-5 samples indicate that the effective positron traps are vacancy clusters more complex than hexa-vacancies.

Coincidence Doppler Broadening Spectroscopy

The analysis of PALS spectra made it possible to associate the lifetime values τ_1 and τ_2 with different structures acting as effective positron annihilation sites present in each of the studied samples. Under this scenario, a suitable choice of reference CDB spectra would provide a specific way to enhance the information related to preferential presence of some type of defects among all those revealed by PALS in each sample. For this reason, we present the CDBS results as CDB ratio curves relative to the UO-2 and UO-5 samples, respectively. In particular; the sample UO-2 has an oxygen to uranium concentration ratio near the stoichiometry composition. On the other hand, in the sample UO-5 practically all the defect structure is composed of large vacancy clusters, as positron annihilation is near a saturation state ($I_2 \sim 94\%$).

CDB ratio curves relative to the UO-2 sample

In Fig. 7, CDB ratio curves obtained for all samples studied relative to the CDB spectrum of the UO-2 sample are shown. Specifically, the use of UO-2 as a reference sample enhances the signal coming from positron annihilated inside the bigger vacancy clusters.

From the analysis of the results presented in Fig. 7, similar features can be seen in the CDB ratio curves obtained for the samples grown at different oxygen partial pressure ratios (UO-4 and UO-5). Specifically, for these samples at a longitudinal momentum p_L equal to 0 corresponds to a ratio value around 1.05; then a pronounced valley is observed at around 12×10^{-3} m_0c with a ratio value of about 0.8, followed by a peak around 15×10^{-3} m_0c. For higher p_L values, a second well-defined peak
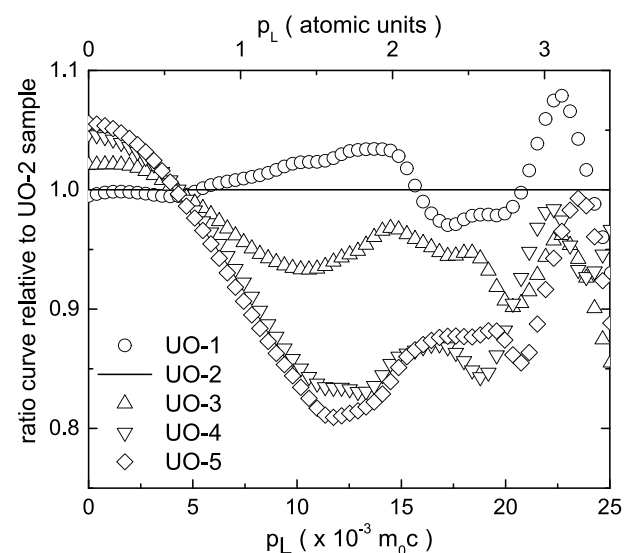
Fig. 7. CDBS ratio curves relative to that obtained from the UO-2 sample.

can be observed for $p_L \sim 22.5 \times 10^{-3}$ m_0c.

To give an accurate support to the interpretation of our experimental results, we have used results recently reported of first principle calculations of the momentum distributions of the annihilating electron–positron pairs in vacancy-like defects in a UO_2 perfect lattice [22]. In this paper, the authors calculated the different momentum distributions for uranium vacancies and different $V_U + V_O$ complexes (the mono-vacancy V_U and di- to hexa-vacancy $V_U + V_O$ complexes) in UO_2. In order to allow a direct comparison with experimental results, Wiktor *et al.* convoluted the calculated momentum distributions with a Gaussian function having a FWHM of 1.2 keV [22]. Then, the results were reported as ratio curves using as reference the momentum distribution calculated for the perfect lattice.

It must be pointed out that our CDB ratio curves obtained for the UO-4 and UO-5 samples are qualitatively in good agreement with the simulated ratio curves reported by Wiktor *et al.* [22]. In particular, these authors attributed the momentum distribution characterized by the peak around $p_L = 0$ and the pronounced valley around 10×10^{-3} m_0c followed by a second peak, to a strong localization of the positron wave function in a uranium vacancy (V_U) of the vacancy clusters. Based on the CDBS results for the UO-4 and UO-5 samples we can assert that in the vacancy clusters identified by PALS (see Section Positron Lifetime Spectroscopy) the positron signal mainly comes from positrons annihilated in uranium vacancies. Consequently, and in agreement with calculation results, the positron wave function must be strongly localized in the uranium vacancies of the vacancy clusters with no or a slight overlapping with the electrons of the neighbor oxygen atoms. In the case of the CDB ratio curve obtained for the UO-1 sample, at $p_L = 0$ the ratio value is slightly below 1 and a broad peak exists around 12×10^{-3} m_0c. The shape of this curve is typical of positron annihilation in oxides [50,51], or in oxygen precipitates [52], when positrons annihilate with oxygen atoms. As can be seen, the CDB ratio curve corresponding to the UO-3 samples is in-between those obtained for the UO-1, UO-4, and UO-5 samples.

Summarizing, the CDB ratio curves presented in Fig. 7 show a direct evidence on the progressive change in the defect structure going from UO-5 to UO-1 samples and indicate that there is a prevalent localization of the positron wavefunction inside uranium vacancies of the vacancy clusters and positron annihilation near oxygen related defects.

CDB ratio curves relative to the UO-5 sample

In Fig. 8, CDB ratio curves obtained for all samples studied relative to
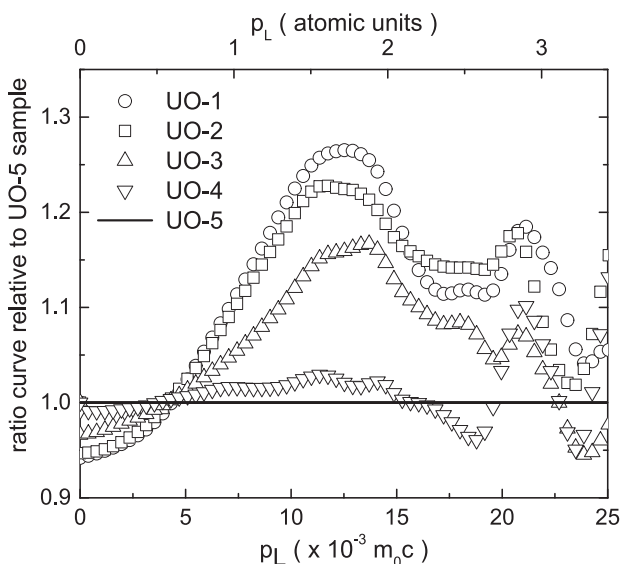

Fig. 8. CDBS ratio curves relative to that obtained from the UO-5 sample.

the CDB spectrum of the UO-5 sample are shown. Specifically, the use of UO-5 as a reference sample is made in order to strongly reduce the contribution of the signal of positron annihilation in uranium vacancies and, consequently, to enhance the signal related to negatively charged oxygen defects.

From the analysis of the CDB ratio curves presented in Fig. 8, at a longitudinal momentum component p_L equal to 0, the ratio values for all the samples are systematically below 1. Besides, the value of this parameter in the low momentum region progressively decreases following the sequence from the UO-4 to the UO-1 samples. For higher momentum values, all CDB ratio curves qualitatively show the same shape which is characterized by a broad peak around 12×10^{-3} m_0c, and a well-defined peak at $p_L \sim 22.5 \times 10^{-3}$ m_0c. It can also be seen that in the high p_L region the intensity systematically evolves with increasing ratio values according to the sequence from UO-4 to UO-1 samples. In particular, when analyzing the p_L region around 12×10^{-3} m_0c a wide peak corresponding to the UO-4 sample can be seen; then this peak becomes narrower and more intense following the sequence from UO-3 to UO-1 samples. As already mentioned in Section CDB ratio curves relative to the UO-2 sample, this effect is attributed to positron annihilation with electrons of oxygen atoms. Furthermore, the peaks for a longitudinal momentum around 22.5×10^{-3} m_0c observed in Figs. 7 and 8 can be ascribed to positron annihilation with high momentum electrons of uranium.

PALS-CDBS: Overall discussion.

On the basis of the results presented in Sections Positron Lifetime Spectroscopy and Coincidence Doppler Broadening Spectroscopy, a discussion considering the different UO_x film growing conditions is given below. The analysis of CDBS curves of Figs. 7 and 8 has pointed out the presence of annihilation of positrons with oxygen atoms and strong localization at positrons in uranium vacancies of the vacancy clusters. The CDBS signal from positron annihilation with oxygen is expected to be originated mainly by annihilation with negatively charged oxygen defects of different nature [16,17,22]. Anyway, a contribution to this signal due to annihilating positrons in clusters and whose wavefunctions slightly overlap with neighboring oxygen cannot be completely ruled out. This unambiguous signal coming from annihilation with oxygen strengths the interpretation (Section Positron Lifetime Spectroscopy) of lifetime τ_1 reflecting annihilation with oxygen related defects, but a closer look at the trend of intensity I_1 shows that, in some cases, it is not directly correlated to the trend in the CDBS signal due to positron annihilation with oxygen.

In the series UO-2, UO-4, UO-5 produced at increasing O_2 partial pressure and keeping the substrate temperature at 400 °C, di-, tri vacancy clusters and larger clusters were detected in sample UO-2, UO-4, and UO-5, respectively. Vacancy clusters increase both in size as in quantity going from UO-2 to UO-5, and conversely the intensity I_1 of annihilation with oxygen atoms decreases on the average from $\sim 26\%$ to 5%. The trend of I_1 is in complete agreement with that of the intensity in the CDBS signal (see Fig. 8). In this series of samples, we can assert that the formation of large vacancy clusters is followed by a strong decrease of oxygen related defects, nevertheless of the fact that the O_2 partial pressure increases during the film deposition.

The effect of the substrate temperature induces a different trend in the family of defects. In samples UO-1 and UO-2, di- and tri- vacancies are present. Increasing the temperature of the substrate at 600 °C, sample UO-3, less but large vacancy clusters appear. The intensity I_1 of annihilation with oxygen atoms (differently than in the UO-2, UO-4, UO5 series) increases on the average from 17% to 33% while the CDBS signal has an opposite behavior decreasing from UO-1 to UO-3 sample (see Fig. 8). This behavior would indicate that some other type of defects not related to oxygen contributes to the lifetime τ_1. These defects, like the lifetime coming from annihilation with negatively charged oxygen, would have a lifetime slightly higher than the bulk lifetime. We can exclude a contribution to τ_1 from uranium mono-vacancies and small

clusters because their lifetimes range from 300 ps to above [21]. Oxygen vacancies could be considered. Although some authors considered more likely the formation of positively charged oxygen vacancies [16,17]; neutral or negatively charged oxygen vacancies, predicted to have a lifetime around 200 ps [21], remain possible candidates.

Conclusions

The results of measurements with Positron Annihilation Spectroscopies on DC magnetron sputtered hyperstoichiometric uranium oxide thin films have been presented. Three depth profiling techniques were employed: PALS, DBS and CDBS. The depth distribution of defects was obtained by DBS. In particular, the combination of PALS and CDBS made it possible to indicate the different types of defects when comparing with recent theoretical calculations. The positron probe was found to be very sensitive to the uranium vacancy in vacancy clusters and to negatively charged oxygen defects. Since positrons localize mainly in a uranium vacancy the lifetime values are less sensitive to the different types of vacancy clusters. Despite that, by comparing with theoretical calculations, we have established a range of possible vacancy clusters that are present in the samples obtained with specific preparation conditions. On the other side, CDBS shows to be very sensitive to small changes in the type of defects, the presence of oxygen defects and possibly the overlapping of the wavefunction of positron localized in a cluster with the neighboring oxygen. Further theoretical calculations of the momentum distribution of positron–electron annihilation pairs in uranium oxygen defects would be needed to extract more detailed information from the experimental CDBS curves.

CRediT authorship contribution statement

C. Macchi: Investigation, Software, Formal analysis, Visualization, Writing - review & editing. **A. Somoza:** Conceptualization, Investigation, Methodology, Writing - original draft, Funding acquisition. **J. Guimpel:** Resources, Writing - review & editing. **S. Suárez:** Resources, Writing - review & editing. **W. Egger:** Resources. **C. Hugenschmidt:** Conceptualization, Resources, Writing - review & editing, Funding acquisition. **S. Mariazzi:** Writing - review & editing. **R.S. Brusa:** Conceptualization, Investigation, Methodology, Writing - original draft, Funding acquisition.

Declaration of Competing Interest

The authors declare that they have no known competing financial interests or personal relationships that could have appeared to influence the work reported in this paper.

Acknowledgments

References

[1] Olander DR. J. Nucl. Mater. 1998;252:121.

[2] Leduc J, Gönüllü Y, Ruoko T-P, Fischer T, Mayrhofer L, Tkachenko NV, et al. Adv. Funct. Mater. 2019;29:1905005.

[3] Adamska AM, Lawrence Bright E, Sutcliffe J, Liu W, Payton OD, Picco L, et al. Thin Solid Films 2015;597:57.

[4] Feldman J W and Mayer L C 1986 Fundamentals of Surface and Thin Film Analysis, 1986, North Holland.

[5] Nitzki V, Hj M. Phys. Rev. 1973;8:1894.

[6] Hj M. J. Nuc. Mat. 1999;270:49.

[7] Garcia P, Fraczkiewicz M, Davoisne C, Carlot G, Pasquet B, Baldinozzi G, et al. J. Nucl. Mater. 2010;400:112.

[8] Cooper MWD, Murphy ST, Andersson DA. J. Nucl. Mater. 2018;504:251.

[9] White JT, Nelson AT. J. Nucl. Mater. 2013;443:342.

[10] Andersson DA, Uberuaga BP, Nerikar PV, Unal C, Stanek CR. Phys. Rev. B 2011;84: 054105.

[11] Djourelov N, Marchand B, Marinov H, Moncoffre N, Pipon Y, Bérerd N, et al. J. Nucl. Mater. 2013;443:562.

[12] Djourelov N, Marchand B, Marinov H, Moncoffre N, Pipon Y, Nédélec P, et al. J. Nucl. Mater. 2013;432:287.

[13] Dorado B, Garcia P, Carlot G, Davoisne C, Fraczkiewicz M, Pasquet B, et al. Phys. Rev. B 2011;83:035126.

[14] Wang J, Eing RC, Becker U. Sci. Rep. 2014;4:4216.

[15] Dorado B, Jomard G, Freyss M, Bertolus M. Phys. Rev. B 2010;82:035114.

[16] Crocombette J-P. Phys. Rev. B 2012;85:144101.

[17] Vathonne E, Wiktor J, Freyss M, Jomard G, Bertolus M. J. Phys.: Condens. Matter 2014;26:325501.

[18] Yu J, Bai X-M, El-Azab A, Allen TR. J. Chem. Phys. 2015;142:094705.

[19] Palomares R, McDonnell M, Yang L, Yao T, Szymanowski JES, Neufeind J, et al. Phys. Rev. Mat. 2019;3 053611.

[20] Crocombette J-P, Torumba D, Chartier A. Phys. Rev. B 2011;83:184107.

[21] Wiktor J, Barthe M-F, Jomard G, Torrent M, Freyss M, Bertolus M. Phys. Rev. B 2014;90:184101.

[22] Wiktor J, Jomard G, Torrent M, Bertolus M. J. Phys.: Condens. Matter 2017;29: 035503.

[23] Hautojärvi P. Positrons in Solids. Heidelberg: Springer-Verlag; 1979.

[24] Brandt W, Dupasquier A. Positron solid-state physics. Amsterdam: North-Holland Publ; 1983.

[25] Sperr P, Egger W, Kögel G, Dollinger G, Hugenschmidt C, Repper R, et al. Appl. Surf. Sci. 2008;255:35.

[26] Gigl T, Beddrich L, Dickmann M, Rienäcker B, Thalmayr M, Vohburger S and C. Hugenschmidt 2017 New Journal of Physics 19 123007.

[27] Pardo F, Burmeister G, Guimpel J. Rev. Sci. Instrum. 1996;67:2370.

[28] Kiessig H. Ann. Phys. 1931;402:769.

[29] Feldman L C and Mayer J W 1986 Fundamentals of surface and thin film analysis (Amsterdam: North-Holland).

[30] Limandri S, Olivares C, Rodriguez L, Bernardi G, Suárez S. Nucl. Instrum. Methods B 2014;318:47.

[31] Mayer M 1999 SIMNRA, Computer simulation of RBS, ERDA and NRA Max-Planck Institut für Plasma Physik.

[32] Hugenschmidt C, Löwe B, Mayer J, Piochacz C, Pikart P, Repper R, et al. Nucl. Instrum. Methods A 2008;593:616.

[33] Schultz PJ, Lynn KG. Rev. Mod. Phys. 1988;60:701.

[34] Kirkegaard P, Pedersen NJ, Eldrup M. Computer code PATFIT-88 (RISO-M-2740) Risoe Natl. Roskilde: Lab; 1989.

[35] Stadlbauer M, Hugenschmidt C, Schreckenbach K, Böni P. Phys. Rev. B 2007;76: 174104.

[36] Alatalo M, Kauppinen H, Saarinen K, Puska MJ, Mäkinen J, Hautojarvi P, et al. Phys. Rev. B 1995;51:4176.

[37] Alatalo M, Barbiellini B, Hakala M, Kauppinen H, Korhonen T, Puska MJ, et al. Phys. Rev. B 1996;54:2397.

[38] Asoka-Kumar P, Alatalo M, Ghosh VJ, Kruseman AC, Nielsen B, Lynn KG. Phys. Rev. Lett. 1996;77:2097.

[39] Čížek J. J. Mater. Sci. & Technol. 2018;34:577.

[40] Stadlbauer M, Hugenschmidt C, Schreckenbach K. Appl. Surf. Sci. 2008;255:136.

[41] Reiner M, Pikart P, Hugenschmidt C. J. Phys. Conf. Ser. 2013;443:012071.

[42] Dupasquier A, Kögel G, Somoza A. Acta Mater. 2004;52:4707.

[43] Brusa RS, Deng W, Karwas GP, Zecca A. Nucl. Instrum. and Meth. B 2002;194:519.

[44] van Veen A, Schut H, de Vries J, Hakvoort RA, Ijpma MR. Proc. Positron Beams for Solids and Surfaces. New York: AIP; 1990.

[45] Brusa RS, Duarte Naia M, Zecca A, Nobili C, Ottaviani G, Tonini R, et al. Phys. Rev. B 1994;49:7271.

[46] Brusa RS, Karwasz GP, Tiengo N, Zecca A, Corni F, Tonini R, et al. Phys Rev. B 2000;61:10154.

[47] Lyczkowski RW. Nuclear chemical engineering. New York: McGraw-Hill Book Company; 1981.

[48] Krause-Rehberg R, Leipner HS. Positron Annihilation in Semiconductors-Defect Studies, (Springer Series in Solid State Science). (Berlin: Springer-Verlag); 1999.

[49] Barthe M-F, Labrim H, Gentils A, Desgardin P, Corbel C, Esnouf S, et al. Phys. Status Solidi C 2007;4:3627.

[50] Brusa RS, Macchi C, Mariazzi S, Karwasz GP, Egger W, Sperr P, et al. Phys. Rev. B 2005;71:245320.

[51] Hugenschmidt C, Pikart P, Schreckenbach K. Phys. Status Solidi C 2009;6:2459.

[52] Brusa RS, Deng W, Karwasz GP, Zecca A, Pliszka D. Appl. Phys. Lett. 2001;79:1492.